Enhanced Microstructural and Performance Characteristics of Cu–18 Pct Ag Composites Through Elemental Additions

XIAO GUO, LIN ZHANG, DAOQI ZHANG, YUNCHAO LI, and ENGANG WANG

Cu–Ag *in-situ* composites, renowned for their amalgamation of high strength and superior electrical conductivity, find extensive applications as conductors in high field magnets. This investigation delves into the microstructural intricacies and mechanical characteristics of Cu–18 pct Ag (wt pct) *in-situ* composites following the incorporation of alloying elements (Nb, Cr, and Zr) *via* a comprehensive process involving casting, heat treatment, and cold deformation. The outcomes reveal that the introduction of Nb or Cr elements intricately refines the Cu dendrites and eutectic phase. Simultaneously, the Cu matrix experiences fortification through the inclusion of Nb or Cr particles, imparting notable improvements in mechanical properties. Remarkably, Cr addition exhibits the most pronounced impact on elevating both ultimate tensile strength and hardness. Under a deformation rate (η) of 5.28, the ultimate tensile strength surges by 21.00 pct compared to that of the Cu–18 pct Ag alloy, albeit with a marginal 7.36 pct decrease in conductivity for the Cu–18 pct Ag–1 pct Cr alloy. The introduction of Nb augments ultimate tensile strength by 12.23 pct, with no apparent impact on conductivity under identical deformation conditions. In contrast, Zr addition significantly disrupts the precipitation of the Ag phase, fostering the formation of the intermetallic compound Cu_4AgZr. This disruption induces a reduction in both mechanical properties and conductivity, leading to embrittlement at high drawing strains.

I. INTRODUCTION

COPPER(CU)-BASED composites materials, such as Cu–Ag,[1] Cu–Nb,[2] Cu–Cr,[3] *etc*., find widespread application as conductors in high field magnets, integrated circuits, and lead frames.[4] Notably, Cu–Ag alloy holds particular allure due to its advantageous combination of high strength, superior conductivity, and straightforward fabrication processes. Given that current–magnetic field interactions lead to the generation of Lorentz forces, it becomes imperative for conductor materials to exhibit robust strength properties.[5] Cu–Ag alloy can be deformed *via* rolling or drawing, leading to continuous microstructure refinement and enhanced strength. Nevertheless, the enhancement of mechanical strength of copper alloys is often accompanied by a reduction in electrical conductivity, leading to a trade-off between the two. Attaining the optimal equilibrium between conductivity and strength requires meticulous adjustments in alloy composition,[6] heat treatment,[7] and deformation parameters,[5] constituting the focal point of current research endeavors.[7,8]

The ultimate mechanical properties of Cu–Ag *in-situ* composites hinge on the nanoscale spacing between Ag fibers, a parameter intricately linked with solidification structure and the deformation process.[9] The alloy composition impacts the morphology, distribution, and precipitation of the Ag-rich phase,[10] which determines the mechanical properties and conductivity of Cu–Ag alloy.[11] After deformation processing, the microstructure of Cu–Ag alloy transforms into a filamentous structure,[12,13] where Ag filaments are produced from the Ag-rich eutectic colonies and the Ag precipitations in the Cu dendrites. In Cu–Ag alloy, aging hardening exhibits two distinct precipitation modes: continuous and discontinuous precipitation.[12,14,15] Discontinuous precipitation transforms the Ag solute in the Cu matrix into a rod-shaped precipitated phase near the grain boundary, while the

XIAO GUO, DAOQI ZHANG and YUNCHAO LI are with the Key Laboratory of Electromagnetic Processing of Materials (Ministry of Education), Northeastern University, No. 3-11, Wenhua Road, Shenyang 110819, P.R. China and also with the School of Metallurgy, Northeastern University, Shenyang 110819, P.R. China. LIN ZHANG and ENGANG WANG are with the Key Laboratory of Electromagnetic Processing of Materials (Ministry of Education), Northeastern University. Contact e-mails: zhanglin@epm.neu.edu.cn; egwang@mail.neu.edu.cn

continuous precipitated phase forms a network structure appearing as small particles in a scanning electron microscope image.[14–16]

The microstructure of the as-cast Cu–Ag alloys consists of pre-eutectic Cu dendrites, eutectic colonies predominantly composed of the Ag-rich phase, and Ag-rich precipitates.[17,18] Achieving increased strength necessitates the presence of finer Ag fibers with reduced spacing, which, in turn, requires a decrease in the size and spacing of the Ag phase in the original ingot structure. The size and morphology of the fibers in the deformed composites depend on the microstructure of the as-cast alloy,[16] highlighting the significance of developing novel approaches to enhance the microstructure of Cu–Ag ingots. The addition of a third element to the alloy proves to be an effective means of modifying the microstructure of Cu–Ag ingots.[19]

The incorporation of alloying elements, including Nb,[16,20] Cr,[11,21] Zr,[22,23] Fe,[24,25] and rare-earth,[26] presents an effective approach to modifying the distribution and morphology of the Ag-rich phase. Zhao[20] documented that the incorporation of 0.6 pct Nb into Cu–5.8 pct Ag alloy facilitated the continuous precipitation of Ag, resulting in a 6 pct increase in the strength of the alloy compared to Cu–7.9 pct Ag alloy. In a similar vein, Zhang[8] observed that the tensile strength of Cu–6 pct Ag composite, augmented with 1 pct Cr after cold deformation, surpassed that of the Cu–6 pct Ag binary composite by approximately 23 pct, with negligible conductivity loss. Gaganov et al.[14] reported that alloying Zr promoted the continuous precipitation reaction in Cu–7 pct Ag alloys, leading to increased tensile strength. The addition of 0.1 pct Fe to Cu–26 pct Ag alloy refined eutectic colonies and Ag precipitates,[24] resulting in more than 8 pct enhancement in both tensile strength and yield strength. Incorporating Sc into Cu–3 pct Ag[26] alloy and Cu–6 pct Ag[27] inhibited discontinuous precipitation of Ag, significantly improving hardness after cold deformation at low strain levels without affecting conductivity. While the addition of third elements to Cu–Ag alloy can impact the morphology of Ag filaments and alter the mechanical properties and electrical conductivity of the final in-situ composites, their influence on the deformation process remains uncertain and requires further investigation.

In Cu–Ag alloy, the inevitable dissolution of alloying elements into the Cu matrix at room temperature can result in electron scattering, leading to a reduction in electrical conductivity. Nonetheless, due to their low solubility in copper and tendency to form precipitates that act as small reinforcing particles within the composite, Nb, Cr, and Zr serve as promising candidates for alloying elements in Cu–Ag alloys with enhanced strength and conductivity.[8,28–30]

This paper delves into an exploration of the impact of alloying elements (Cr, Zr, and Nb at a concentration of 1 pct) on the microstructure, electrical conductivity, and mechanical properties of Cu–18 wt pct Ag composite material. The study provides comprehensive insights into the strengthening mechanism and conductive mechanisms operating within the material.

II. EXPERIMENTAL

Pure Cu, Ag, Cr, Zr, and Nb (99.99 pct mass) were used as raw materials to produce Cu–18 pct Ag–1 pct X (X = Cr, Zr, and Nb) alloys. The alloys were prepared by melting the constituent elements at 1200 °C for 5 minutes using a frequency induction furnace. The resulting Cu–Ag–X ingots had dimensions of 25 mm in diameter and 100 mm in length. After an initial homogenization heat treatment at 760 °C for 2 hours, followed by water-quenching, the ingots were subjected to rotary swaging, reducing their diameter to 16 mm. Subsequently, a second heat treatment was conducted at 450 °C for 1.5 hours, after which the rods were swaged further to a diameter of 10 mm. The rods were then cold-drawn using a metal drawing bench, reducing the diameter to 2.5 mm per pass, with an average reduction of approximately 20 pct per pass. Subsequently, the wires underwent additional drawing, resulting in a final diameter of 1.8 mm after annealing at 370 °C for 2 hours. All heat treatments were carried out under an argon atmosphere. The draw out ratio η, representing the shape variable, was defined as the natural logarithm of the ratio of the original cross-sectional area (A_0) to the final cross-sectional area (A), i.e., $\eta = ln(A_0/A)$. In this study, the total drawing strain η was 5.28.

The as-cast and as-drawn samples were prepared by sectioning, polishing, and etching in a solution containing 3 g $FeCl_3$, 2 ml HCl, and 96 ml C_2H_5OH. The microstructures were examined using a HITACHI S4800 field emission scanning electron microscope (SEM) and FEI Tecnai $G^2$20 transmission electron microscopy (TEM). The precipitation kinetics of the solution-treated alloy samples were determined through differential scanning calorimetry, employing heating rates ranging from 10 to 50 °C/min, within a temperature range of room temperature to 550 °C. Microhardness assessments were carried out employing a Shimadzu HMV-2 Vickers hardness tester, utilizing a diamond square-based pyramid subjected to a 100 N load for a duration of 10 seconds. The specimen prepared for the hardness test exhibited a uniformly flat mirror surface devoid of discernible scratches. Hardness testing was conducted using the Shimadzu HMV-2 hardness tester, applying a loading load of 500 g for a duration of 10 seconds. Each sample underwent ten measurements, and the results were averaged. Tensile tests were executed on an INSTRON 5969 testing machine at room temperature, employing a constant tensile rate of 1 mm/min. Tensile specimens with varying strain rates featured wire diameters ranging from 1.8 to 3 mm and a length of 100 mm, as depicted in Figure 1. Electrical resistivity measurements were
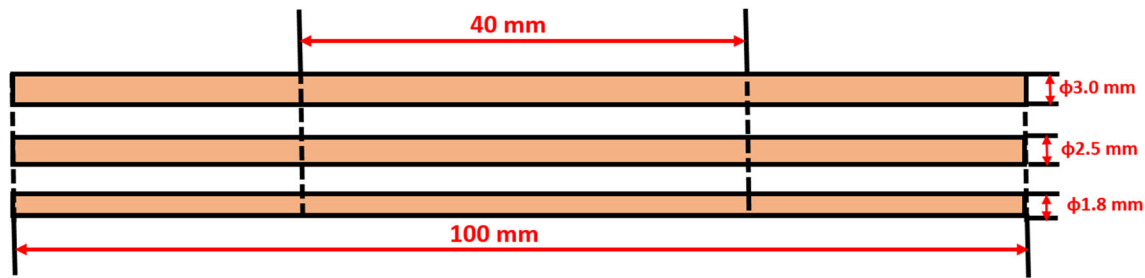
Fig. 1—Dimensions of the tensile specimen.

performed using the standard four-probe method with a Keithley 2450 SourceMeter microhm meter. The electrical conductivity was determined through the application of the standard conversion equation (IACS, 100 pct IACS = 1.7241 $\mu\Omega$ cm).

III. RESULTS AND DISCUSSION

A. Microstructure of As-cast Cu–Ag Alloys

The alloys investigated in this study, namely Cu–Ag–X (X = Cr, Zr, and Nb), had an Ag content (18 pct) that exceeded the limited solubility of Ag in Cu (7.9 pct) at the eutectic temperature of 779 °C, indicating hypoeutectic compositions. The as-cast Cu–18 pct Ag–X alloy exhibited a characteristic hypoeutectic microstructure (Figure 2) comprising a primary Cu-rich phase, eutectic colonies, and Ag precipitates. The eutectic colonies, resulting from residual liquid during solidification, primarily formed along the boundaries of the dendrites. Additionally, a significant number of Ag precipitates were present within the primary Cu-rich phase (Figure 2(b)). The size of the eutectic colonies was determined by the formation process of the Cu phase, which, in turn, was influenced by the shape and size of the Cu dendrites, varying with the addition of different third alloying elements.

In the Cu–18 pct Ag–1 pct Nb alloy, compared to the Cu–18 pct Ag alloy, the size of Cu dendrites was observed to be smaller (Figure 2(c)). Furthermore, the eutectic colonies in the Cu–18 pct Ag–1 pct Nb alloy exhibited a uniform distribution and were surrounded by dendrites. Near the Ag-rich eutectic colonies of the Cu–18 pct Ag–1 pct Nb alloy, the presence of small particles was identified as the Nb-rich phase through EDS analysis (spot 1 in Figure 2(d)). The EDS analysis of spot 1 in Figure 2(d) revealed a particle composition with 24.08 pct Nb, confirming its Nb-rich nature. These Nb-rich particles were observed as randomly distributed white particles within the matrix (Figures 2(d)), and EDS mapping displayed the dispersion of fine Nb particles within the Cu matrix (Figure 4(c)). This observation differed from the findings of Raabe et al.,[31] where Nb predominantly existed in dendritic form in the alloy containing 4 pct Nb. The disparity in observations could be ascribed to the tendency of Nb to exist in the form of tiny particles in alloys with lower Nb content (Figure 3).

In the Cu–18 pct Ag–1 pct Cr alloy, the eutectic colonies exhibited a fine strip network structure (Figure 2(e)), and their shape appeared to be slimmer compared to those in Cu–Ag and Cu–Ag–Nb alloys. The addition of Cr also led to the refinement of Cu dendrites' size. Furthermore, within the eutectic structure, there were black particles of larger size compared to the Nb-rich particles in Cu–Ag–Nb. EDS point analysis (spot 2 in Figure 2(f)) and mapping (Figures 4(d) to (f)) confirmed these black particles to be Cr-rich particles. These Cr-rich particles were primarily distributed in proximity to the eutectic colonies, indicating that they were displaced by the growing Cu dendrites during solidification. The morphology of the Cr-rich particles resembled their distribution in Cu–Cr alloys.[32] Typically, Cr-rich phases in Cu–Cr alloys tend to segregate within the residual liquid during solidification, thus being displaced by growing Cu dendrites and distributed within the interdendritic regions. In this study, the Cr-rich particles were homogeneously distributed in the Cu–18 pct Ag–1 pct Cr alloy (Figures 4(d) and (f)).

In the Cu–18 pct Ag–1 pct Zr alloy, in addition to the eutectic colonies, there were dark-colored Ag-rich regions observed along the dendrite boundaries (Figures 2(g) and (h)). Some of the eutectic colonies appeared to be detached from the network structure. However, the fraction of Ag-rich eutectic colonies was lower compared to the Cu–18 pct Ag alloy, as another etched dark-colored phase occupied certain regions of the grain boundaries. EDS analysis confirmed that the dark-colored compounds were Cu–Ag–Zr compounds (Figure 2(h)). The EDS spectrum matched the elements Cu, Ag, and Zr, and a quantitative evaluation revealed the following element concentrations: 51.06 wt pct (62.51 at. pct) Cu, 32.31 wt pct (23.30 at. pct) Ag, and 16.63 wt pct (14.18 at. pct) Zr (spot 3 in Figure 2(h)). This composition corresponds to the solubility range of the ternary phase Cu_4AgZr.[33, 34] Furthermore, most of the dark-colored Ag-rich regions exhibited an irregular shape in the Cu–18 pct Ag–1 pct Zr alloy (Figure 2(h)). The shape of Cu_4AgZr compounds in the Cu–18 pct Ag–1 pct Zr alloy resembled those observed in previous studies on Cu–3 pct Ag–1 pct Zr,[35] Cu–6 pct Ag–0.2 pct Zr,[22] and Cu–6 pct Ag–1 pct Zr.[8] EDS mapping of the Cu–18 pct Ag–1 pct Zr alloy (Figures 4(g) to (i)) unequivocally identifies light-colored regions as eutectic colonies and the dark-colored phase as the Cu_4AgZr compound.
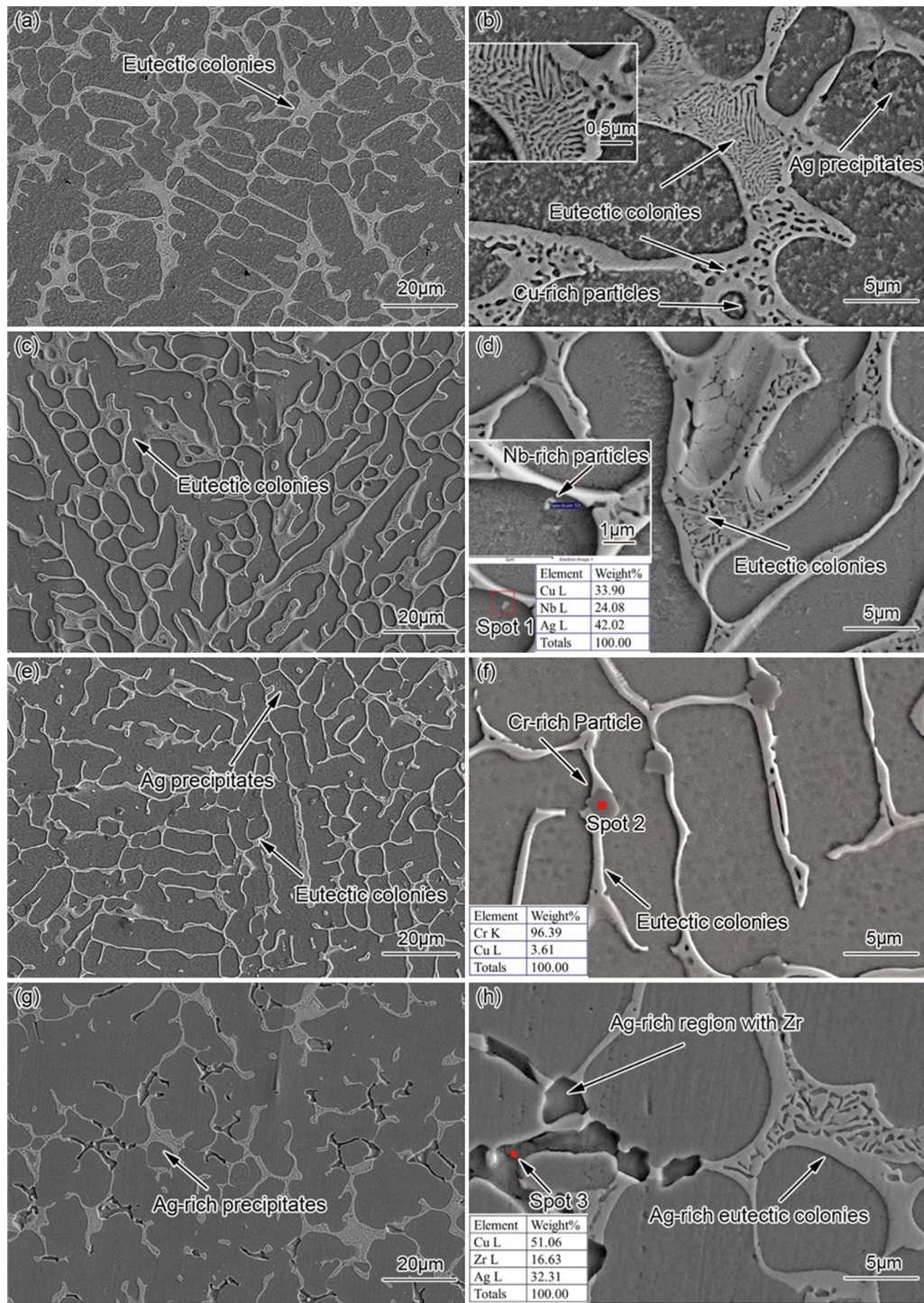
Fig. 2—Field-emission scanning electron microscopy (SEM) images of the as-cast Cu–Ag alloys: (*a*, *b*) Cu–18 pct Ag; (*c*, *d*) Cu–18 pct Ag–1 pct Nb; (*e*, *f*) Cu–18 pct Ag–1 pct Cr; (*g*, *h*) Cu–18 pct Ag–1 pct Zr.

As presented in Table I, the incorporation of third elements resulted in a decrease in the thickness of eutectic colonies in Cu–18 pct Ag alloys. Furthermore, the addition of Nb or Cr elements led to a reduction in the mean interval between eutectic colonies, whereas the addition of Zr element increased the mean interval. The mean interval of eutectic colonies is influenced by the spacing of dendrites. The introduction of Cr or Nb elements resulted in a decrease in dendrite spacing, consequently affecting the average intervals of eutectic colonies. In this study, the dendrite spacing under consideration is specifically the secondary dendrite spacing. The determination of dendrite spacing λ can be achieved using the Kirkwood equation:[36]

$$\lambda = \left[-\frac{128 D_L \sigma T \ln(C_e/C_0)}{H m_L (1-k)(C_e - C_0)} t_f \right]^{1/3} \qquad [1]$$

The equation involves various parameters including the volumetric heat of fusion (H), interfacial energy (σ), local solidification time (t_f), absolute melt point (T),

Fig. 3—X-ray diffraction (XRD) patterns of the as-cast Cu–Ag alloys.

diffusion coefficient of the liquid phase (D), liquidus slope (m_L), equilibrium distribution coefficient (k), overall alloy composition (C_0), and eutectic concentration (C_e). Notably, the presence of Cr components in Cu–18 pct Ag–1 pct Cr alloys resulted in a significant refinement of the eutectic colonies, which contrasts with the observed coarsening effect in Cu–6 pct Ag alloys upon Cr addition as reported by Liu et al.[11] In our previous research on Cu–6 pct Ag,[8] it was found that the alloying of Cr or Nb promoted Ag solute rejection and led to the coarsening of Cu dendrites. This phenomenon was attributed to the influence of constitutional supercooling. During the solidification process, segregation occurs at the solidification interface due to constitutional supercooling. The low solid solubility of the added elements in the Cu–Ag alloy leads to their enrichment at the solid/liquid interface, resulting in a reduced growth rate of Cu dendrite arms and a delayed solidification process. Consequently, the local solidification time (t_f) is prolonged, and the dendrite spacing (λ) is increased. In Cu–18 pct Ag–1 pct Nb and Cu–18 pct Ag–1 pct Cr alloys, the Cr and Nb atoms tend to nucleate into Cr and Nb dendrites, which hinders the growth of Cu matrix and eutectic, thereby reducing the dendrite spacing. Additionally, the formation of Nb-rich and Cr-rich particles with high melting points during solidification acts as inhomogeneous nucleation sites. This enhanced nucleation rate improves the growth rate of Cu dendrites, leading to a decrease in dendrite
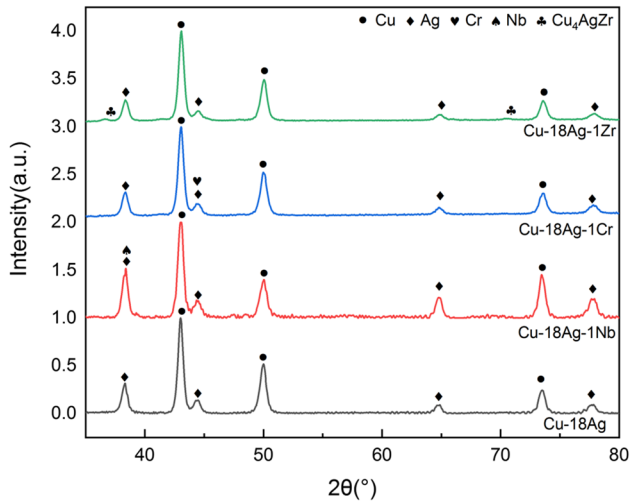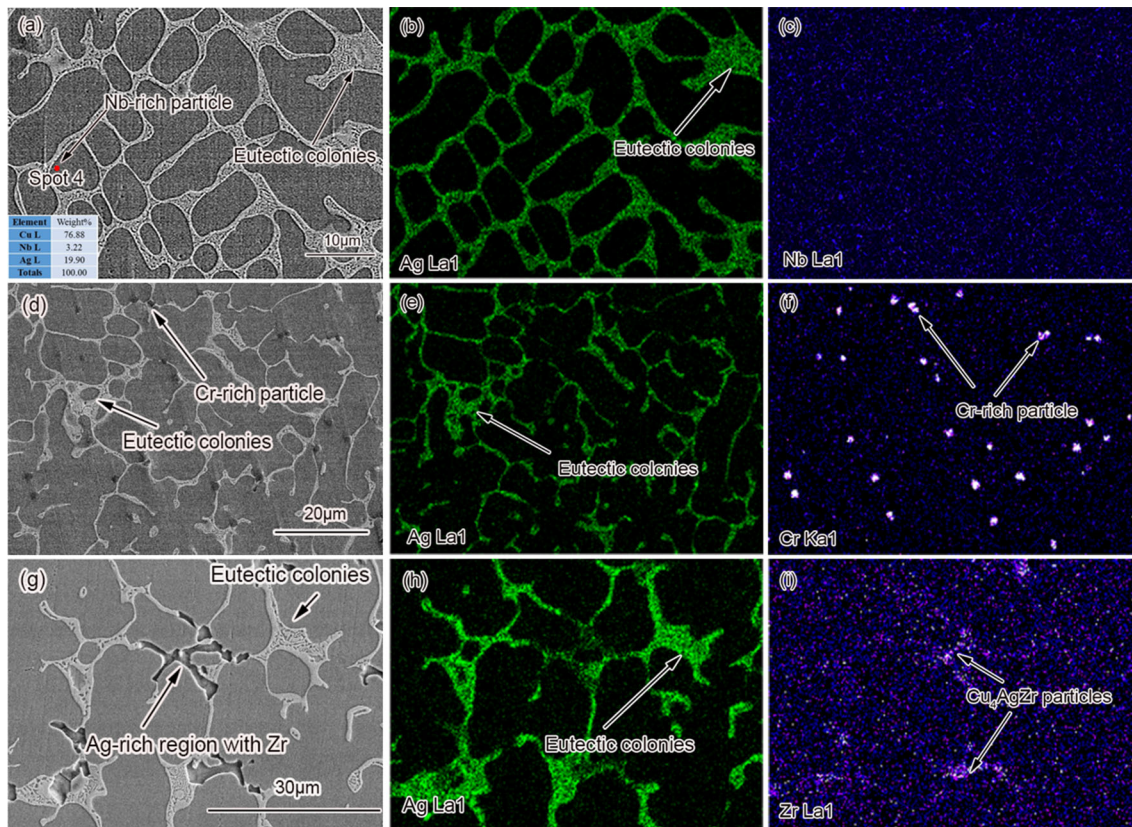

Fig. 4—SEM images and EDS mapping of the as-cast Cu–Ag alloys: (a to c) Cu–18 pct Ag–1 pct Nb alloy; (d to f) Cu–18 pct Ag–1 pct Cr alloy; (g to i) Cu–18 pct Ag–1 pct Zr alloy.

spacing. These findings are consistent with the observations by Liu et al.,[37] who reported a more uniform distribution of the eutectic structure and a smaller average interval between dendritic arms with the addition of 0.1 pct rare-earth element (RE) in Cu–24 pct Ag alloy. Conversely, the addition of 0.1 pct RE to Cu–6 pct Ag alloy led to coarsening of the interval between dendritic arms. Hu[38] documented that incorporating 0.14 pct La into Cu–2 pct Ag alloy enhances the formation of extensive (3 to 5 μm) primary Ag phases in the as-cast Cu–2Ag alloy. Li Rui et al.[25] also demonstrated that the addition of 0.1 pct Fe can reduce the eutectic lamella and dendrites spacing.

In contrast, the addition of Zr element in Cu–18 pct Ag–1 pct Zr alloy leads to the formation of Cu$_4$AgZr compound through a reaction with Cu and Ag. Although this reaction consumes a small portion of Ag in the residual liquid, it does not have a noticeable impact on constitutional supercooling and dendrite spacing. The formation of Cu$_4$AgZr compound occurs at relatively low temperatures and does not serve as nucleation sites, indicating that the addition of Zr does not significantly affect the nucleation of Cu dendrites. However, in the Cu–18 pct Ag–1 pct Zr alloy, the eutectic colonies exhibit a discontinuous distribution and only cover certain parts of the dendrite boundary, resulting in an increased average interval between eutectic colonies.

The X-ray diffraction (XRD) patterns of the as-cast Cu–18 pct Ag alloy were analyzed, and it was observed that the addition of Nb and Cr had no significant impact on the XRD patterns (Figure 3). Despite the inclusion of only 1 pct Nb and Cr in the Cu–18 pct Ag alloy, the peak intensities corresponding to Nb and Cr were negligible compared to those of Cu and Ag. Additionally, it should be noted that the main peak of BCC-Cr at $2\theta = 44.4$ deg and the main peak of BCC-Nb at $2\theta = 38.4$ deg might be obscured by the peak of FCC-Ag. Furthermore, the XRD results revealed the presence of peaks corresponding to the Cu$_4$AgZr intermetallic compound in the Cu–18 pct Ag–1 pct Zr alloy, specifically at $2\theta = 36.5$ and 70.5 deg.

The Cu–18 pct Ag alloy, after undergoing solid solution treatment, was analyzed using differential scanning calorimetry (DSC) with various heating rates (Figure 5). It was observed that in samples subjected to higher heating rates, the exothermic peaks shifted toward higher temperatures. These findings are in line with previous studies conducted on Cu–Ag alloys.[20] The DSC curves obtained at different heating rates exhibited distinct peak values, which occurred within the temperature range of 350 °C to 450 °C. These peak values indicated the precipitation of Ag within the Cu matrix. Moreover, as the heating rate increased, the peak value gradually shifted toward higher temperatures, which is consistent with the characteristic behavior observed in DSC heating curves.

According to the equation proposed by Kissinger,[39]

$$\ln \frac{b}{T_p^2} = -\frac{E_a}{RT_p} + C \qquad [2]$$

The parameter b represents the heating rate, T_P corresponds to the peak temperature observed in the DSC curve for various heating rates, R represents the ideal gas constant, and C is a constant. The maximum value of the derivative at temperature was determined by calculating the local exothermic peak. Figure 5(b) illustrates Kissinger's diagram, which was used to calculate the activation energy of the reaction for the four alloys. By substituting this result into the equation, the activation energy (Ea) for the precipitation of Ag can be obtained and is presented in Table II. The DSC results provide insights into the activation energy of the Ag precipitation reaction during non-isothermal processes. It was observed that the activation energy of the ternary alloys was lower than that of the Cu–18 pct Ag alloy. This suggests that the addition of elements facilitated the precipitation of the precipitated phase during heating, leading to a reduction in the precipitation activation energy of the Cu matrix.

In previous studies, DSC was employed to calculate the activation energy of the Ag precipitation reaction in different Cu–Ag alloy systems. For instance, the activation energy of the Ag precipitation reaction in Cu–4 wt pct Ag–3 wt pct A1 alloy was determined to be 66.6 kJ/mol.[40] In the case of Cu–7wt pct Ag alloy, the calculated activation energy was found to be 99 kJ/mol.[41] For the discontinuous precipitations in Cu–5.8 pct Ag–0.6 pct Nb alloy, the activation energy value was reported as 63 ± 5 kJ/mol.[20] Furthermore, the activation energy of Cu–28 pct Ag was measured as 129.1 ± 20.7 kJ/mol,[42] while the addition of 0.1 pct Fe in Cu–26 pct Ag resulted in an activation energy of 129 ± 8.9 kJ/mol.[24] It is worth noting that this higher value might be attributed to the elevated Ag content in the system. In this study, the addition of Cr or Nb elements in the Cu–18 pct Ag alloy resulted in even lower activation energies for the precipitation of Ag compared to the aforementioned research. The lower activation energies favor the promotion of Ag precipitation.

B. Microstructural Evolution of Composites upon Wire Drawing

Microstructural analysis of the Cu–18 pct Ag–1 pct X composites after wire drawing was conducted using SEM. Figure 6 presents the longitudinal section micrographs of Cu–18 pct Ag–1 pct X alloys at strain levels of $\eta = 3.22$ and 4.18. The microstructural features of these Cu–Ag wires included a Cu-rich phase (dark-colored) along with thin Ag-rich filaments and relatively thick Ag-rich lamellae (light-colored). It was observed that the Ag filaments/lamellae were aligned parallel to the stretching direction due to the applied strain. The formation of Ag-rich lamellae originated from the eutectic colonies present in the solidification microstructure. The eutectic colonies in the Cu–18 pct Ag alloy gradually underwent alignment along the drawing direction, resulting in a fiber-like microstructure. This behavior is consistent with previous findings reported

Table I. Mean Thickness, Interval, and Area Fraction of Eutectic Colonies in Cu–Ag Alloys

Alloy Composition	Mean Thickness (μm)	Mean Interval (μm)	Area Fraction (Pct)
Cu–18 Pct Ag	1.46	6.07	22.24
Cu–18 Pct Ag–1 Pct Nb	1.37	5.37	29.21
Cu–18 Pct Ag–1 Pct Cr	1.23	5.41	16.26
Cu–18 Pct Ag–1 Pct Zr	0.14	9.62	20.63
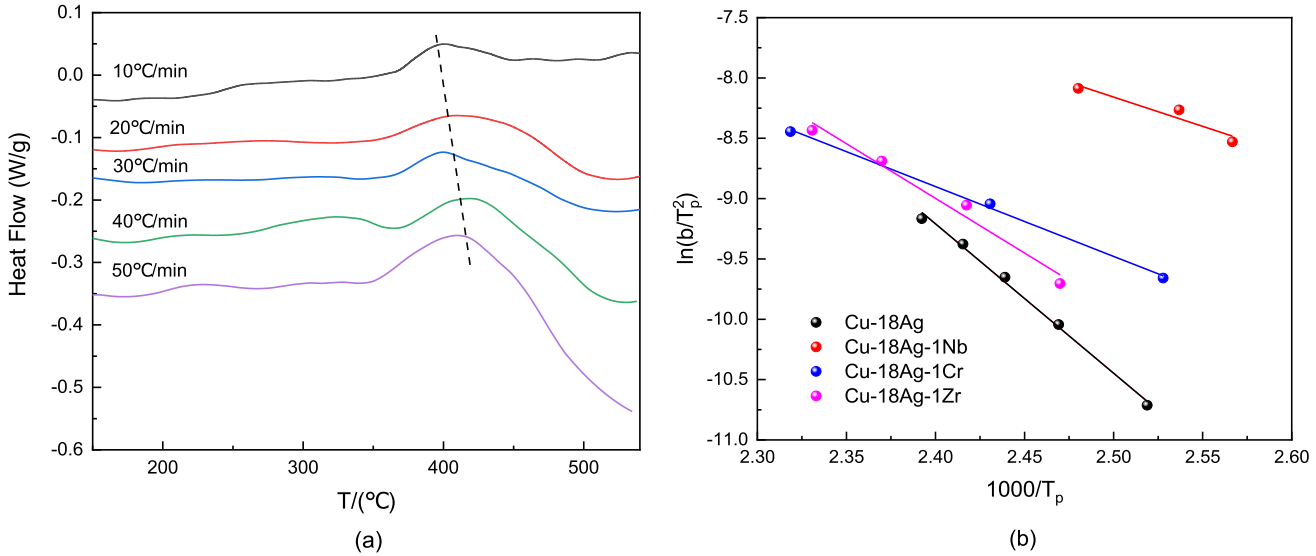
Fig. 5—Differential scanning calorimetry (DSC) results of the solution-annealed Cu–18 pct Ag alloy: (*a*) DSC curves obtained at different heating rates in Cu–18 pct Ag alloys; (*b*) Kissinger diagram utilized for the calculation of the activation energy of the reaction.

Table II. Activation Energy (E_a) for the Precipitation of Ag in Cu–18 pct Ag–1 Pct X Alloys

Alloy Composition	The Precipitation Activation Energy (E_a) /kJ/mol
Cu–18 Pct Ag	102.95 ± 3.82
Cu–18 Pct Ag–1 Pct Nb	40.34 ± 11.96
Cu–18 Pct Ag–1 Pct Cr	48.12 ± 2.37
Cu–18 Pct Ag–1 Pct Zr	75.83 ± 8.17

for Cu–28 pct Ag alloys.[43] Notably, both Cu and Ag possess the face-centered cubic (FCC) crystal structure and share similar slip systems, leading to comparable rheological stress and hardening characteristics between the two metals. Consequently, during the cold working process, the Cu dendrites and eutectic regions exhibit coordinated deformation, promoting uniform elongation of the two phases parallel to the drawing direction, as well as uniform shrinkage in the direction perpendicular to the drawing direction.

The cross-sectional analysis of deformed Cu–Ag wires at two strain levels is presented in Figure 7. The Cu-rich α-phase (dark-colored phase) and Ag-rich eutectic colonies (represented by the thick Ag-rich lamellae) maintained their original shapes, resembling the solidification microstructure. However, the fine Ag-rich filaments exhibited a particle-like appearance in the cross-sections, as they were aligned along the wire axis due to the strain-induced drawing. These filaments originated from the Ag-rich precipitates within the Cu matrix. It was observed that the spacing and thickness of the Ag-rich filaments/lamellae decreased with increasing tensile strain. Furthermore, the incorporation of Cr and Nb elements led to a reduction in both the spacing and size of the Ag filaments and Ag lamellae.

A uniform microstructure with elongated grain structure was observed in the *in-situ* composites of Cu–18 pct Ag, Cu–18 pct Ag–1 pct Nb, and Cu–18 pct Ag–1 pct Cr at a significant deformation level (Figures 6(a) to (f)). Compared to the Cu–18 pct Ag wires, the Cu–18 pct Ag–1 pct Nb and Cu–18 pct Ag–1 pct Cr wires exhibited relatively thinner Ag lamellae (Figures 6(a), (c), and (e)). The shape of Cr-rich particles in the deformed rods/wires remained similar to that in the as-cast state,
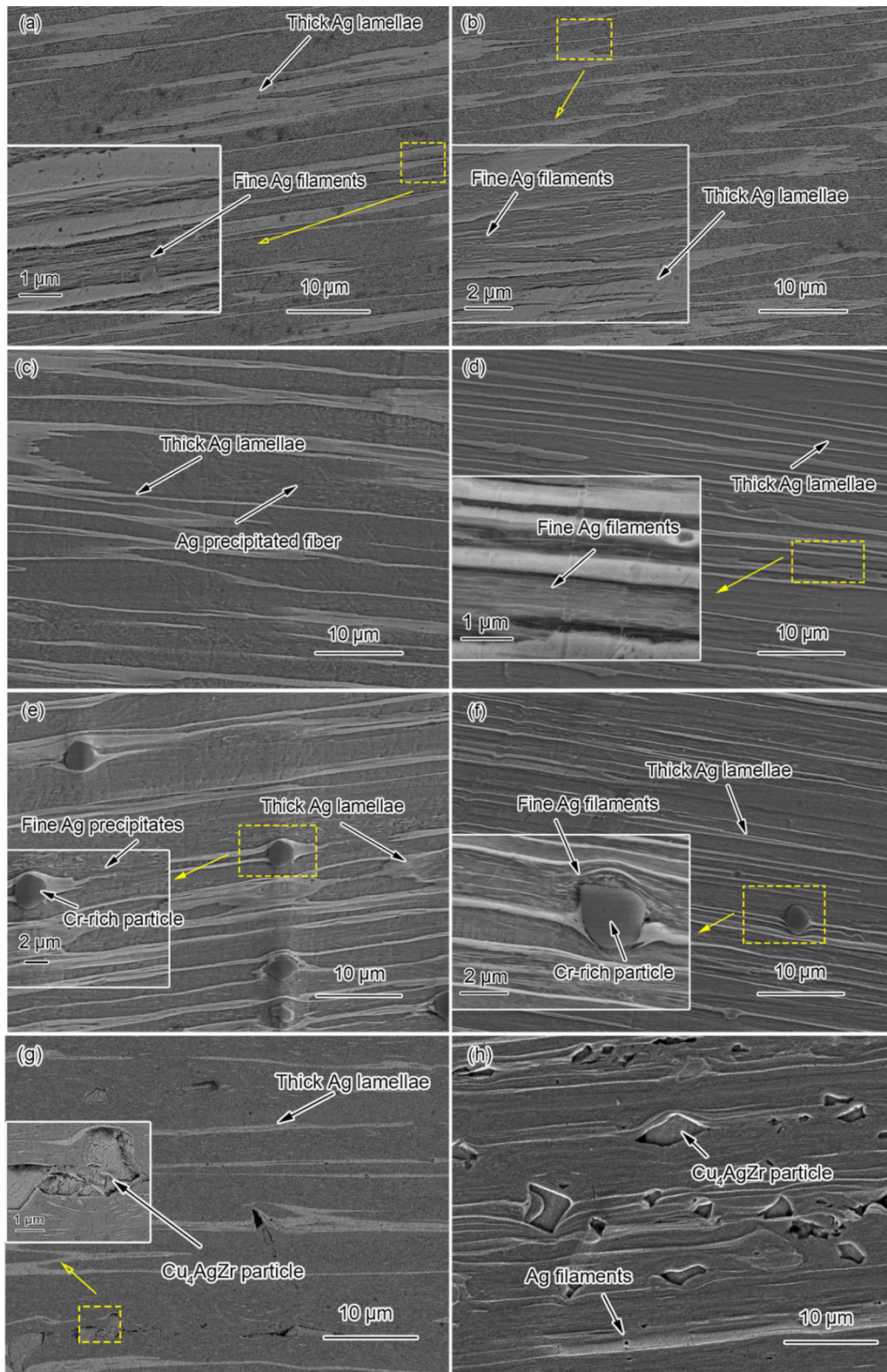
Fig. 6—Longitudinal section SEM images of Cu–Ag composites at different drawing strains. (*a*, *b*) Cu–18 pct Ag at $\eta = 3.22$ and $\eta = 4.18$, respectively; (*c*, *d*) Cu–18 pct Ag–1 pct Nb at $\eta = 3.22$ and $\eta = 4.18$, respectively; (*e*, *f*) Cu–18 pct Ag–1 pct Cr at $\eta = 3.22$ and $\eta = 4.18$, respectively; (*g*, *h*) Cu–6 pct Ag–1 pct Zr at $\eta = 3.22$ and $\eta = 4.18$, respectively.

suggesting their resistance to deformation. During the drawing process of the rods/wires, the presence of Cr hindered the development of certain Ag-rich filaments/ lamellae, thereby enhancing strain hardening in the neighboring regions. Furthermore, the Cu–18 pct Ag–1 pct Zr composites displayed distinct Cu$_4$AgZr particles,
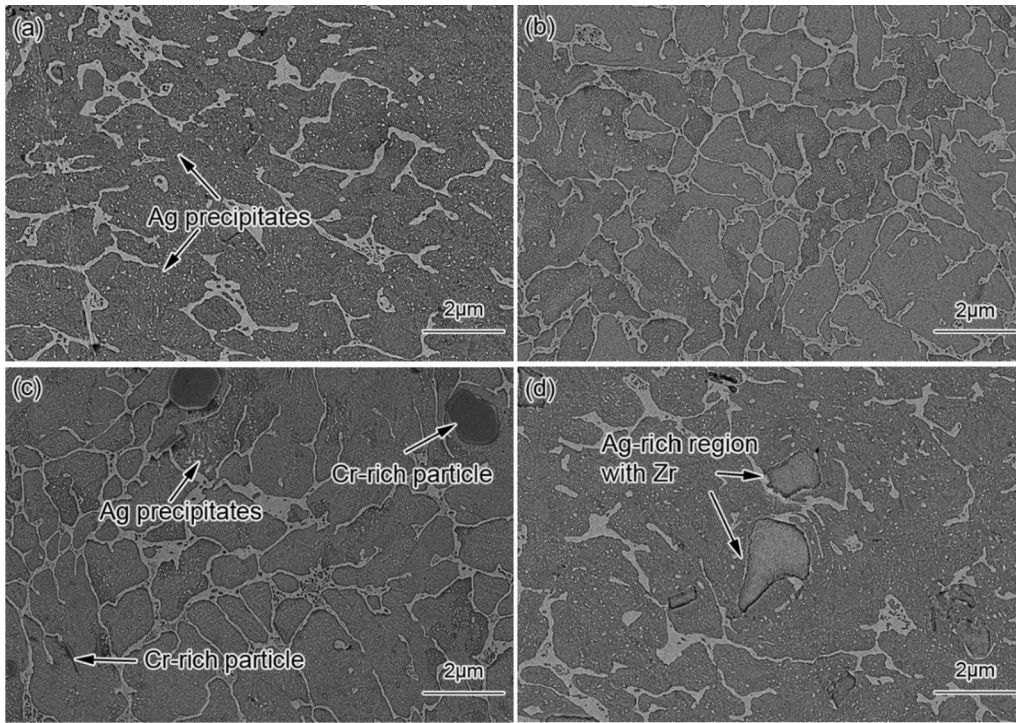
Fig. 7—SEM images of the cross section of the Cu–Ag composites at a drawing strain of $\eta = 3.22$ (*a*) Cu–18 pct Ag; (*b*) Cu–18 pct Ag–1 pct Nb; (*c*) Cu–18 pct Ag–1 pct Cr; (*d*) Cu–18 pct Ag–1 pct Zr.
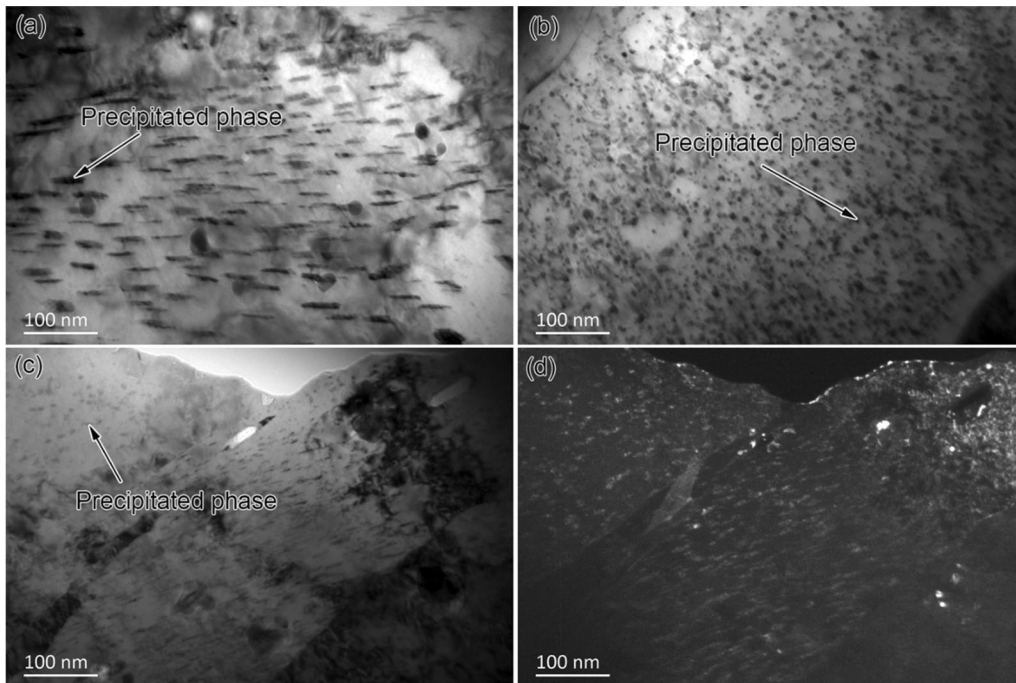
Fig. 8—TEM images of the longitudinal section of the deformed Cu–Ag composites at a strain of $\eta = 3.22$. (*a*) Cu–18 pct Ag; (*b*) Cu–18 pct Ag–1 pct Zr ; (*c*) Cu–18 pct Ag–1 pct Cr (bright-field image); (*d*) Cu–18 pct Ag–1 pct Cr (dark-field image).

thick Ag-rich lamellae, and fine filaments (Figures 6(g) and (h)). However, the length of the Ag fibers was shorter, and their quantity was lower compared to the other three alloys. As previously mentioned, the addition of Zr resulted in the formation of Cu_4AgZr compound particles in the Cu–18 pct Ag–1 pct Zr alloy, causing the Ag fibers surrounding the Cu_4AgZr compound particles to exhibit curvature. Additionally, the

TEM images in Figure 8 revealed a larger number of nanoscale Ag precipitates in the alloys with $\eta = 3.22$, and the size of these precipitates in the Cr-added and Zr-added specimens was smaller than that in the Cu–18 pct Ag alloy. These precipitates are likely corresponding to the Ag filaments depicted in Figure 6. The calculated results of activation energy for precipitation as presented in Table II demonstrate that the incorporation of Cr, Nb, and Zr into the Cu–18 pct Ag alloy results in a reduction of the activation energies associated with Ag precipitation. This phenomenon effectively facilitates the initiation of Ag nano-phases precipitation. Such a phenomenon holds potential in achieving a finer distribution of Ag precipitates, thus distinguishing it from the behavior observed in binary Cu–18 pct Ag alloys. In the Cu–18 pct Ag–1 pct Cr alloy, small bright spots indicating nanoscale Ag precipitated phases appear in the dark-field image (Figure 8(d)). A comparative analysis of the morphological characteristics of the observed Ag precipitates in TEM images presented in Figure 8 supports the validity of the calculated activation energy results.

C. *Mechanical and Electrical Properties of the Composites*

Figure 9 delineates the alterations in the electrical properties of the Cu–18 pct Ag–X alloy with varying degrees of deformation. The properties of the alloys exhibit a gradual evolution corresponding to the microstructural changes. The conductivity of the alloys shows a slight decrease with increasing drawing strain. Cr addition results in a 5 to 12 pct reduction in conductivity compared to the base Cu–18 pct Ag alloy. This decrement is smaller than that reported for the Cu–6 pct Ag–1 pct Cr alloy, where the addition of Cr resulted in a conductivity reduction of 12 to 18 pct.[21] The conductivity of the Cu–18 pct Ag–1 pct Nb alloy is slightly lower than that of the Cu–18 pct Ag alloy at low strain levels, while it becomes comparable to the Cu–18

pct Ag alloy at high strain levels. With increasing deformation degree, the conductivity of the Cu–18 pct Ag–1 pct Zr alloy significantly decreases. The higher melting point of Zr necessitates higher melting temperatures during the preparation of Cu–18 pct Ag–1 pct Zr alloys, increasing the likelihood of oxygen and other impurity incorporation, which consequently decreases the conductivity. Furthermore, as the deformation increases, the morphology of the intermetallic compounds Cu_4AgZr exhibits no significant change with respect to the matrix tensile state, while defects manifest within the matrix. Impurities and defects have detrimental effects on the electrical conductivity of the Cu–18 pct Ag–1 pct Zr alloy. Additionally, Zr forms Cu_4AgZr compounds with Cu and Ag, occupying a higher volume fraction compared to Cr and Nb, and these compounds exhibit lower conductivity. The conductivity of the Cu–Ag composites further increases at a strain of $\eta = 5.28$. This can be attributed to the effect of intermediate annealing (370 °C, 2 hours) following a deformation degree of $\eta = 4.61$. In the Cu–18 pct Ag alloy containing eutectic fibers, a continuously distributed network forms, exerting a strong scattering effect on electrons. In alloys with a certain eutectic structure, the primary factor contributing to the formation of alloy resistivity is the barrier to electron conduction caused by interfacial scattering between the eutectic fiber bundle and the Cu matrix fiber. The presence of the third phase refines the eutectic colonies and increases their quantity, thereby enhancing the number of barriers to electron conduction and increasing the resistivity of the alloy. Residual undissolved third-phase remnants within the matrix further contribute to the increased resistivity of the alloy.

The resistivity of Cu–Ag composites can generally be attributed to four scattering mechanisms, as described by previous research:[44]

$$\rho_{Cu-Ag} = \rho_{imp} + \rho_{dis} + \rho_{int} + \rho_{pho}, \qquad [3]$$

where ρ_{imp} is impurities scattering, ρ_{dis} is dislocation scattering, ρ_{int} is interface scattering, and ρ_{pho} is phonon scattering. The electrical conductivity of Cu–18 pct Ag–X alloys is primarily influenced by the microstructure of the Cu matrix, the presence of Ag-rich precipitates and eutectic colonies, and the resistivity of other phases in the alloy. In Cu–Ag alloys, there are two types of Cu/Ag interfaces: one between Ag and Cu dendrites and the other between Ag precipitates and the Cu matrix.[43] As deformation increases, the Cu/Ag interface undergoes elongation and an increase in density, resulting in increased electron scattering due to interface scattering. Consequently, ρdis and ρint are the primary factors contributing to the decrease in electrical conductivity with increasing deformation. Zhang[21] attributed the increase in resistivity with strain to the enhanced scattering of conducting electrons at the Cu/Ag phase interface, especially when the spacing between filaments decreases to a similar magnitude as the mean free path of conducting electrons. An[6] associates the decline in Cu–Ag–Sc alloy conductivity with reduced Ag fiber spacing, leading to heightened interfacial scattering
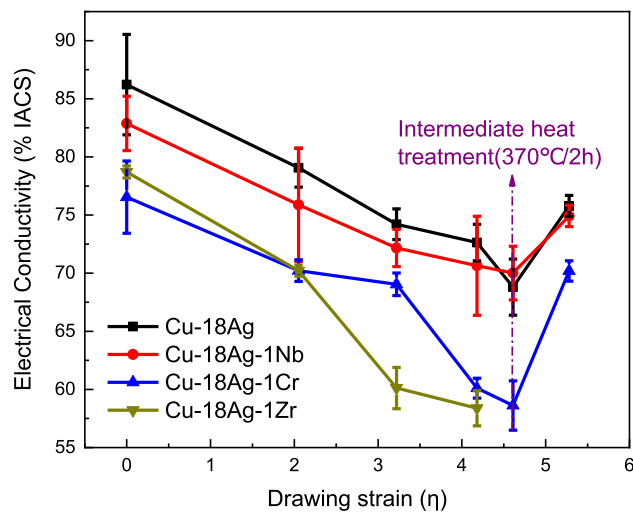

Fig. 9—Variation of conductivity in Cu–18 pct Ag alloy with different elements as a function of the degree of deformation.

(ρ_{int}). In a deformed alloy, the decrease in conductivity is partly attributed to the increase in dislocation density during deformation, leading to an increase in ρdis. The presence of small amounts of third elements (Cr, Nb, and Zr) dissolved in the matrix enhances the scattering of electrons by point defects, thereby increasing ρimp. ρ_{pho} represents the scattering of electrons by lattice vibrations, primarily influenced by temperature and decreasing rapidly with decreasing temperature. This scattering contribution remains relatively constant during cold drawing.[11]

The conductivity of Cu–18 pct Ag–1 pct X alloys, in comparison to Cu–18 pct Ag, is relatively lower, primarily due to the differences in the distribution of filaments within the alloys. The transmission of electrons through filamentary bundles in the alloys encounters more significant scattering at phase interfaces within these bundles, leading to increased resistance. Through an appropriate intermediate heat treatment, the supersaturated Ag phase present in the Cu matrix undergoes precipitation. While solid-soluble atoms in Cu–18 pct Ag alloy contribute to resistance reduction, the addition of a third component results in a higher proportion of the low-conductive phase compared to the binary alloy. As a consequence, there is a slight decrease in resistivity.

Figure 10 illustrates the mechanical property variations of the deformed Cu–18 pct Ag–X composites at different drawing strains. Contrary to the trend observed in electrical conductivity, the hardness of the four composite materials monotonically increased with the increase in tensile strain. A comparison between Cu–18 pct Ag alloy and Cu–18 pct Ag–1 pct Nb and Cu–18 pct Ag–1 pct Zr alloys revealed only slight differences in hardness. However, Cu–18 pct Ag–1 pct Cr alloy exhibited a significant increase in hardness after deformation, indicating that the addition of Cr resulted in enhanced strain hardening. At a deformation of 4.61, the hardness of Cu–18 pct Ag–1 pct Cr alloy reached

241.33 HV, representing a 9.5 pct increase compared to Cu–18 pct Ag.

Figure 10(b) presents the variations in the ultimate tensile strength (UTS) of Cu–18 pct Ag–X alloys with respect to the deformation degree. The experimental UTS values are represented by the plotted columns. In the deformation range of 4.18 to 4.61, the UTS of the Cu–18 pct Ag–X alloys increased as the deformation degree increased. However, when the deformation reached 4.61, the Cu–18 pct Ag–1 pct Zr alloy exhibited poor plasticity and could not continue to be drawn, resulting in significantly lower strength compared to the other alloys. This indicates that the addition of 1 pct Zr had a detrimental effect on the strength of Cu–Ag alloys. Furthermore, with increasing deformation, the strength of Cu–18 pct Ag and Cu–18 pct Ag–1 pct Cr alloys exhibited a slight decrease after intermediate annealing (370 °C, 2 hours) at a deformation of 4.61. At a drawing strain of 4.61, the UTS of the Cu–18 pct Ag–1 pct Cr alloy was 152 MPa higher than that of the Cu–18 pct Ag composite. Although the drawing strain for both Cu–18 pct Ag–1 pct Cr and Cu–18 pct Ag alloys increased from 4.61 to 5.28, the hardness and UTS decreased after intermediate annealing. At a deformation rate of $\eta = 5.28$, the ultimate tensile strength of Cu–18 pct Ag–1 pct Cr increased by 21.00 pct compared to that of the Cu–18 pct Ag alloy. The addition of Nb slightly increased the UTS of the Cu–18 pct Ag–1 pct Nb alloy at low drawing strains, and when the strain was increased to 5.28, the addition of Nb enhanced the ultimate tensile strength by 12.23 pct.

The mechanical characteristics of the Cu–18 pct Ag–X alloy substantially surpass those of the Cu–6 pct Ag–X alloy.[8] In the Cu–6 pct Ag–X alloys, the eutectic colonies are separated and have a particle-like shape, whereas the eutectic colonies in the Cu–18 pct Ag–X alloys exhibit a reticular structure. With increasing drawing strain, the reticular eutectic colony undergoes
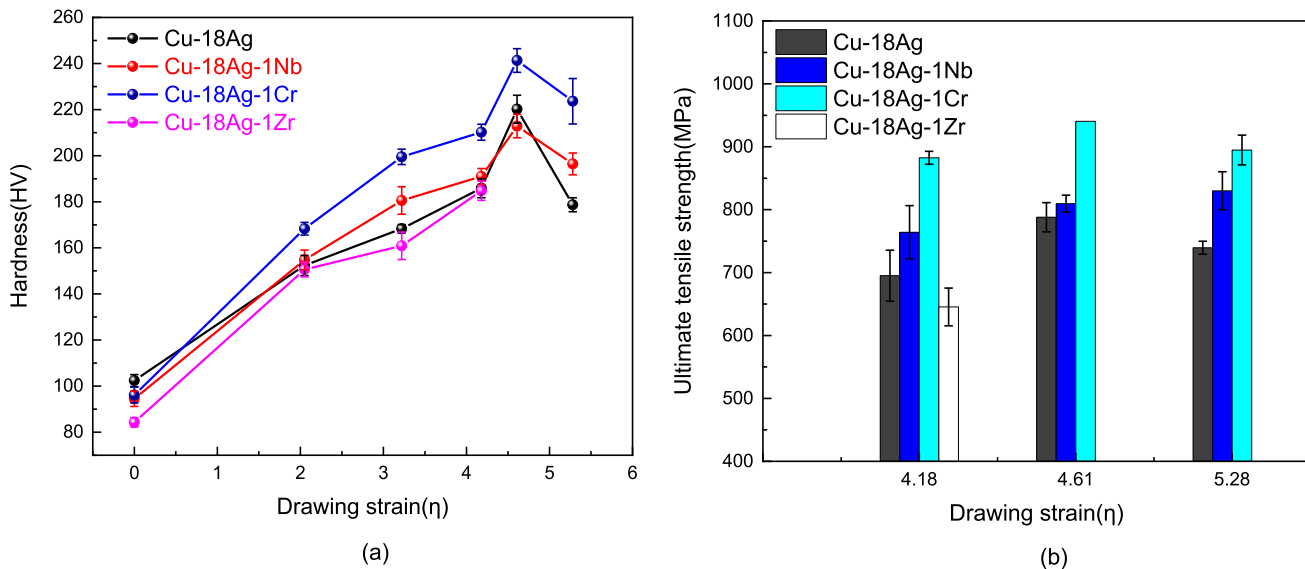

Fig. 10—Variation of mechanical properties in deformed Cu–Ag composites at different drawing strains: (a) measured hardness; (b) measured ultimate tensile strength.

deformation and transforms into a fibrous form. The Cu–18 pct Ag alloys demonstrate superior strain hardening due to their higher Ag content. Moreover, the alloying effect of the third element on hardness becomes more pronounced with increasing Ag content in Cu–Ag alloys. The addition of the third element results in a uniform distribution of Ag fibers in the microstructure and refines the fiber thickness. This imparts a dispersion strengthening effect, enhancing the mechanical properties of the alloy.

Ag plays a crucial role as the primary strengthening factor in Cu–Ag alloy, existing in various forms such as eutectic colonies, precipitated phase, and solid solution. However, the introduction of Zr to the Cu–18 pct Ag alloy results in the formation of the metal compound Cu_4AgZr, which consumes a portion of Ag. This Cu_4AgZr compound exhibits a significantly larger size compared to the Ag fibers depicted in Figure 6, diminishing its effectiveness as reinforcing particles. Consequently, the inclusion of Zr diminishes the work hardening ability of the alloy. The optimal Zr percentage as an effective reinforcing element in the Cu–Ag-Zr composition necessitates further exploration, considering that a minor addition of less than 0.1 pct already enhances the strength of the Cu alloy by altering the precipitation mode of Ag.[14] Conversely, the addition of Nb and Cr elements contributes to the regular arrangement of Ag fibers and refines both the Cu and Ag phases, leading to further improvement in the work hardening ability. Among the three elements, Cr demonstrates the most pronounced effect on increasing the strength of the Cu–18 pct Ag alloy. This enhancement can be attributed to the precipitation mechanism, which plays a significant role in grain strengthening.[20,29]

The rule of mixture (ROM) is designed to predict the properties of composites consisting of simple mixtures. Still, in our case, the small spacing of the reinforcing phase, akin to fine crystal grains, aligns more with the Hall–Petch law.[45] The rule of mixture is limited to cases where the reinforcing phase size is relatively large. When the internal dimensions of the alloy reach the nanometer scale, the actual strength of the alloy is far higher than the calculated value of the rule of mixture.[46] By using the rule of mixture to estimate the strength of various composite materials with pure Cu and Ag values, the estimated values would be significantly lower than the actual measured values. Adopting the Hall–Petch equation[47] for strength calculations is akin to adding the effects of grain size or phase boundaries to the ROM calculations. Many researchers in similar composite materials, such as Cu–Ag,[48,49] Cu–Nb,[50] and Ag–Ni,[51] have employed the Hall–Petch effect to calculate the impact of the reinforcing phase on alloy strength. The Hall–Petch equation is expressed as follows:

$$\sigma = \sigma_{ROM} + k\lambda^{-1/2} \qquad [4]$$

Here, σ_{ROM} is the frictional internal stress and k is the Hall–Petch coefficient. Given that the volume fraction of the Ag phase is significantly greater than that of the

third component, and the spacing is considerably smaller than the grain size of the Cu matrix, it can be assumed that the Ag phase predominantly contributes to the overall strength through the Hall–Petch effect. λ represents the spacing between silver wires, with the average distance defined as the separation between these fibers on a transverse section. Han et al.[52] proposed an expression for the Hall–Petch relationship in Cu–Ag composite materials subjected to strain:

$$\sigma = \sigma_{ROM} + k\lambda_0^{-1/2} \exp(\varepsilon/4) \qquad [5]$$

Again, σ_{ROM} is the frictional internal stress and k is the Hall–Petch coefficient. Due to the significantly larger volume fraction of the Ag phase compared to Cr, Nb, or Zr, it can be assumed that the Ag phase predominantly contributes to the overall strength through the Hall–Petch effect. λ_0 represents the spacing between fibers, with the average distance defined as the separation between these fibers on a transverse section.

The strength of Cu–Ag alloy arises from several strengthening mechanisms, including interface strengthening, dislocation strengthening, solid solution strengthening, and precipitation strengthening.[17] In the case of deformable Cu–18 pct Ag–X alloy, the strength is predominantly influenced by the strain intensification of the Cu matrix and the eutectic phase. Consequently, based on the principle of mixing, the deformation strength of the alloy can be expressed as:[52]

$$\sigma = (1 - V_{eut})\sigma_{Cu} + V_{eut}(\sigma_{eut}), \qquad [6]$$

where V_{eut} is the volume fraction of the eutectic phase, σ_{Cu} is the strength of the initial crystal, and σ_{eut} is the strength of the eutectic phase. As the degree of deformation increases, both the eutectic phase and the fiber structure within the Cu–Ag alloy experience work hardening at comparable rates. The strength of the eutectic phase, σ_{eut}, can be described by the Hall–Petch relationship:[44,46]

$$\sigma_{eut} = \sigma_{0(Ag)} + k_{eut}\lambda_{eut}^{-1/2} \exp(\varepsilon/4), \qquad [7]$$

where $\sigma_{0(Ag)}$ is the strength of pure Ag, k_{eut} is the Hall–Petch coefficient, ε is the drawing strain, and λ_{eut} is the lamellar spacing of the eutectic. Owing to the disparate atomic dimensions and shear moduli of Ag and Cu, the incorporation of Ag into Cu induces a strengthening effect on the Cu matrix through solid solution mechanisms. Consequently, the strength of the Cu–Ag alloy can be evaluated by considering both the strength of the Cu matrix and that of the eutectic phase, as articulated in the subsequent equation. The strength of the Cu matrix encompasses strain strengthening resultant from Cu matrix deformation and solid solution strengthening induced by the presence of Ag solute and a third element within the Cu matrix. The strength of the Cu matrix after deformation can be described as

$$\sigma_{Cu} = \sigma_{0(Cu)} + k_{Cu}\lambda_{Cu/Ag}^{-1/2}\exp\left(\frac{\varepsilon}{4}\right)$$
$$+ G\left(|\delta| + \frac{1}{20}|\eta|\right)^{3/2}\sqrt{\frac{\chi_a}{3}} \qquad [8]$$

In the equation, $\sigma_{0(Cu)}$ represents the strength of pure Cu, $k_{Cu/Ag}$ denotes the strengthening coefficient of the Cu matrix, λ_{Cu-Ag} corresponds to the distance of the precipitated Ag phase in the Cu matrix at a given strain, G represents the shear modulus, δ represents the lattice distortion factor, η represents the change factor of the shear modulus, and χ_a represents the atomic fraction of the solute solid dissolved in the Cu matrix. The dominant constituents contributing to the strength of the Cu matrix are precipitation strengthening from the Ag precipitated phase and solid solution strengthening facilitated by Ag atoms in Cu. During the initial stages of deformation, the eutectic phase in the alloy forms a network structure, which gradually transforms into a fibrous form as the drawing strain increases. This deformation process leads to a reduction in the size of Cu and Ag grains, resulting in decreased values of λ_{eut} and λ_{Cu-Ag}. As a result, both the strength of the eutectic phase and the Cu matrix increase. As the degree of deformation further increases, the strength of Cu–Ag alloys continues to rise. Additionally, the addition of Cr and Nb refines the Cu grains and Ag fibers, leading to further reductions in λ_{eut} and λ_{Cu-Ag}, thereby improving the strength of Cu–Ag–X alloys. The presence of Cr-rich and Nb-rich particles in the microstructure also contributes to the mechanical strengthening, although their number and volume fraction are relatively small. However, due to the high Ag content, the transformation of Ag fibers from eutectic colonies plays a dominant role in enhancing the strength through fiber strengthening.

Figure 11 presents stress–strain curves depicting various Cu–Ag composites at a strain of η = 5.28. Notably, the Cu–18 pct Ag–1 pct Cr composite demonstrates a yield strength (YS) of 774.2 MPa, which is significantly higher than that of the Cu–18 pct Ag composite (668.5 MPa). Additionally, the Cu–18 pct Ag–1 pct Nb composite exhibits a YS of 668.7 MPa, slightly surpassing that of the Cu–18 pct Ag composite. These findings underscore the enhanced strength and ductility of the Cu–18 pct Ag–1 pct Nb alloy in comparison to the Cu–18 pct Ag alloy. Intriguingly, the incorporation of Cr diminishes the ductility of the Cu–18 pct Ag composite while markedly enhancing its strength owing to the formation of Cr-rich particles.

The estimated ultimate tensile strength (UTS) values for the three alloys (Cu–18 pct Ag, Cu–18 pct Ag–1 pct Nb, Cu–18 pct Ag–1 pct Cr) with a deformation rate of 5.28 were calculated to be 520, 595, and 609 MPa, respectively, based on Eq. [6]. However, these values deviated from the actual measurements. Upon analyzing the separate contributions to the strength of each alloy, as summarized in Table III, it was found that precipitation strengthening played a dominant role in enhancing the mechanical properties. The improvements in mechanical properties achieved by the addition of Cr and Nb were attributed to their influence on microstructure refinement.

In Figure 12, the correlation between strength and electrical conductivity is elucidated for four alloys, including other high Ag alloys subjected to diverse deformation treatments. In contrast to Cu–18 pct Ag, Cu–18 pct Ag–1 pct Cr exhibited sustained higher strength at approximately 900 MPa while upholding a conductivity of 70 pct IACS. Similarly, Cu–18 pct Ag–1 pct Nb alloy showcased a strength approximately 100 MPa higher than Cu–18 pct Ag alloy, paired with a conductivity of 75 pct IACS. The comprehensive performance of these three alloys surpasses that of several other high-silver alloys reported in the literature,[25,53,54] and with lower Ag content, they offer a cost-effective alternative. Conversely, the substantial presence of Cu₄AgZr in Cu–18 pct Ag–1 pct Zr alloy, due to heightened Zr content, resulted in diminished strength and conductivity, accompanied by reduced plasticity. These revelations underscore the potential applications of Cu–Ag-Cr and Cu–Ag-Nb alloys in conductor coil applications.

In summary, Cu–18 pct Ag–1 pct Cr alloy exhibits superior overall performance compared to the other three alloys. It demonstrates a significant increase in strength and hardness under large deformation, while experiencing only a slight decrease in conductivity. Specifically, at a drawing strain of 5.28, the Cu–18 pct Ag–1 pct Cr wires exhibit a room temperature ultimate tensile strength (UTS) of 895 MPa, a hardness of 224 HV, and a conductivity of 70.19 pct IACS.

IV. CONCLUSION

This investigation delves into the microstructural intricacies and mechanical characteristics of Cu–18 pct Ag *in-situ* composites post the introduction of alloying elements (Nb, Cr, and Zr). This comprehensive process, inclusive of casting, heat treatment, and cold deformation, led to the following conclusions based on the findings:
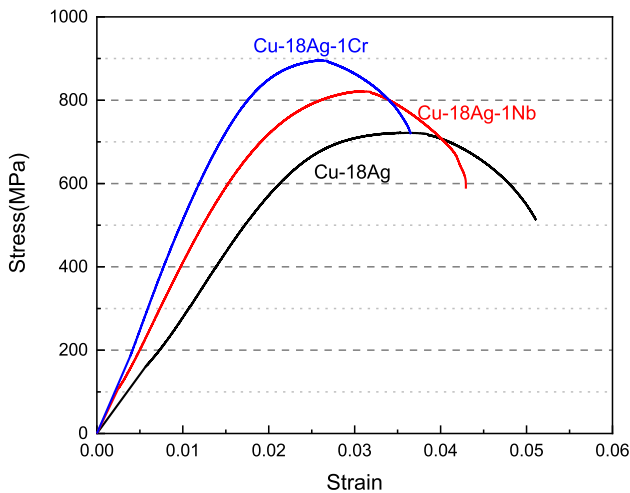
Fig. 11—Stress–strain curves of Cu–18 pct Ag–1 pct X wires under a deformation rate of 5.28.

Table III. Contribution of Individual Factors to the Overall Strength of Cu–18 Pct Ag–1 Pct X Wires Under a Deformation Rate of 5.28

	Cu–18 Pct Ag	Cu–18 Pct Ag–1 Pct Nb	Cu–18 Pct Ag–1 Pct Cr
$\sigma_{0(Cu)}$	20	20	20
Strength of Eutectic Phase	42	69	71
Solid Solution Enhancement	133	136	138
Precipitation Enhancement	345	390	400
Calculated Total Strength	520	595	609
Measured Strength	668	689	774
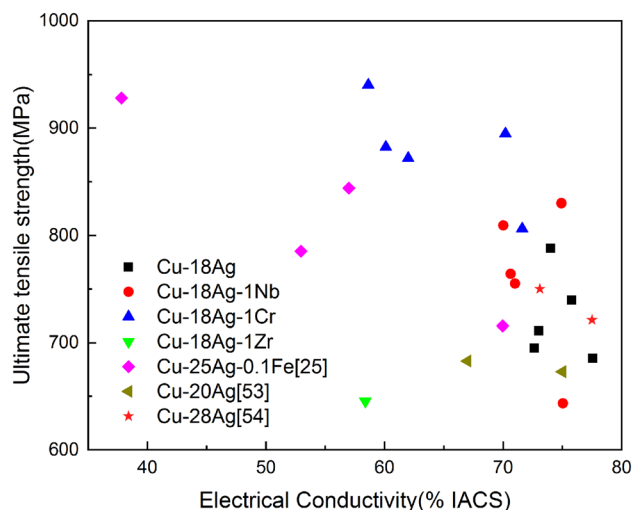
Fig. 12—The relationship between strength and conductivity.

(1) The introduction of Nb and Cr in the Cu–18 pct Ag alloy resulted in the formation of Nb-rich and Cr-rich particles, respectively, within the as-cast microstructure, refining the Cu dendrites and eutectic phase. On the other hand, the addition of Zr led to the formation of Cu_4AgZr compound particles, resulting in an increased average interval between eutectic colonies.

(2) During the wire drawing deformation, Ag precipitates transformed into Ag filaments, and Ag eutectic phase changed into Ag lamellae. The incorporation of Cr and Nb improved the morphology and distribution of Ag fibers in the deformed Cu–18 pct Ag *in-situ* composites, resulting in a reduction in the size and spacing of Ag filaments and Ag lamellae.

(3) The strength and hardness of Cu–Ag–Cr and Cu–Ag–Nb composites were found to be higher than those of the binary Cu–Ag composite under high drawing strains, with only a slight decrease in conductivity. Noteworthy is the surge in ultimate tensile strength by 21.00 pct under a deformation rate (η) of 5.28 for the Cu–18 pct Ag–1 pct Cr alloy compared to the Cu–18 pct Ag alloy, albeit with a slight conductivity reduction of 7.36 pct. The introduction of Nb enhanced the ultimate tensile strength by 12.23 pct without significantly affecting conductivity at the same deformation rate. However, the inclusion of Zr in the

Cu–18 pct Ag alloy resulted in reduced hardness, tensile strength, and electrical conductivity.

These findings underscore the potential of Cu–Ag–Cr and Cu–Ag–Nb composites as promising materials, showcasing improved mechanical properties while maintaining acceptable levels of conductivity, providing a viable option for conducting coils in high magnetic fields.

COMPETING INTERESTS

The authors declare that they have no known competing financial interests or personal relationships that could have appeared to influence the work reported in this paper.

REFERENCES

1. H. Zhao, H. Fu, M. Xie, and J. Xie: *Vacuum*, 2018, vol. 154, pp. 190–99. https://doi.org/10.1016/j.vacuum.2018.05.010.
2. G. Radnóczi, E. Bokányi, Z. Erdélyi, and F. Misják: *Acta Mater.*, 2017, vol. 123, pp. 82–89. https://doi.org/10.1016/j.actamat.2016.10.036.
3. M. Ma, Z. Li, Z. Xiao, H. Zhu, X. Zhang, and F. Zhao: *Mater. Sci. Eng. A*, 2020, vol. 795, p. 140001. https://doi.org/10.1016/j.msea.2020.140001.
4. M. Xie, P. Zhou, W. Huang, H. Chen, L. Gong, W. Xie, H. Wang, and B. Yang: *Mater. Sci. Eng. A*, 2022, vol. 840, p. 143004. https://doi.org/10.1016/j.msea.2022.143004.
5. X. Zhu, Z. Xiao, J. An, H. Jiang, and Z. Li: *J. Alloys Compd.*, 2021, https://doi.org/10.1016/j.jallcom.2021.160769.
6. B. An, R. Niu, Y. Xin, W.L. Starch, Z. Xiang, Y. Su, R.E. Goddard, J. Lu, T.M. Siegrist, E. Wang, and K. Han: *J. Mater. Sci. Technol.*, 2023, vol. 135, pp. 80–96. https://doi.org/10.1016/j.jmst.2022.06.043.

7. K. Song, Y. Geng, Y. Ban, Y. Zhang, Z. Li, X. Mi, J. Cao, Y. Zhou, and X. Zhang: *J. Mater. Sci. Technol.*, 2021, vol. 79, pp. 75–87. https://doi.org/10.1016/j.jmst.2020.11.043.

8. L. Zhang, X. Guo, Z. Li, D. Zhang, and E. Wang: *Metall. Mater. Trans. A*, 2020, vol. 51A, pp. 6727–39. https://doi.org/10.1007/s11661-020-06051-1.

9. X. Guo, L. Zhang, D. Zhang, Y. Li, X. Zhao, and E. Wang: *Mater. Sci. Eng. A*, 2024, vol. 894, p. 146186. https://doi.org/10.1016/j.msea.2024.146186.

10. J. Lyubimova, J. Freudenberger, C. Mickel, T. Thersleff, A. Kauffmann, and L. Schultz: *Mater. Sci. Eng. A*, 2010, vol. 527, pp. 606–13. https://doi.org/10.1016/j.msea.2009.08.036.

11. J.B. Liu, L. Zhang, A.P. Dong, L.T. Wang, Y.W. Zeng, and L. Meng: *Mater. Sci. Eng. A*, 2012, vol. 532, pp. 331–38. https://doi.org/10.1016/j.msea.2011.10.099.

12. W. Grünberger, M. Heilmaier, and L. Schultz: *Mater. Lett.*, 2002, vol. 52, pp. 154–58. https://doi.org/10.1016/S0167-577X(01)00383-4.

13. L. Zhang and L. Meng: *Scr. Mater.*, 2005, vol. 52, pp. 1187–91. https://doi.org/10.1016/j.scriptamat.2005.03.016.

14. A. Gaganov, J. Freudenberger, E. Botcharova, and L. Schultz: *Mater. Sci. Eng. A*, 2006, vol. 437, pp. 313–22. https://doi.org/10.1016/j.msea.2006.07.121.

15. J. Freudenberger, W. Grünberger, E. Botcharova, A. Gaganov, and L. Schultz: *Adv. Eng. Mater.*, 2002, vol. 4, pp. 677–81. https://doi.org/10.1002/1527-2648(20020916)4:9%3c677::AID-ADEM677%3e3.0.CO;2-I.

16. C. Zhao, X. Zuo, E. Wang, R. Niu, and K. Han: *Mater. Sci. Eng. A*, 2016, vol. 652, pp. 296–304. https://doi.org/10.1016/j.msea.2015.11.067.

17. A. Benghalem and D.G. Morris: *Acta Mater.*, 1997, vol. 45, pp. 397–406. https://doi.org/10.1016/S1359-6454(96)00152-8.

18. J. Singh, G. Jerman, R. Poorman, B.N. Bhat, and A.K. Kuruvilla: *J. Mater. Sci.*, 1997, vol. 32, pp. 3891–3903. https://doi.org/10.1023/a:1018604513547.

19. D.G. Morris, A. Benghalem, and M.A. Morris-Muñoz: *Scr. Mater.*, 1999, vol. 41, pp. 1123–30. https://doi.org/10.1016/S1359-6462(99)00262-6.

20. C. Zhao, R. Niu, Y. Xin, D. Brown, D. McGuire, E. Wang, and K. Han: *Mater. Sci. Eng. A*, 2021, vol. 799, p. 140091. https://doi.org/10.1016/j.msea.2020.140091.

21. L. Zhang, L. Meng, and J.B. Liu: *Scr. Mater.*, 2005, vol. 52, pp. 587–92. https://doi.org/10.1016/j.scriptamat.2004.11.035.

22. X. Wu, R. Wang, C. Peng, Y. Feng, and Z. Cai: *Mater. Sci. Eng. A*, 2020, vol. 773, p. 138829. https://doi.org/10.1016/j.msea.2019.138829.

23. X. Wu, R. Wang, C. Peng, and J. Zeng: *Mater. Sci. Eng. A*, 2020, vol. 778, p. 139095. https://doi.org/10.1016/j.msea.2020.139095.

24. R. Li, E. Wang, and X. Zuo: *Materials*, 2017, vol. 10, p. 1383. https://doi.org/10.3390/ma10121383.

25. R. Li, X. Zuo, and E. Wang: *J. Alloys Compd.*, 2019, vol. 773, pp. 121–30. https://doi.org/10.1016/j.jallcom.2018.09.179.

26. B. An, Y. Xin, R. Niu, L. Jun, E. Wang, and K. Han: *Mater. Lett.*, 2019, vol. 252, pp. 207–10. https://doi.org/10.1016/j.matlet.2019.05.101.

27. B.L. An, Y. Xin, R.M. Niu, Z.L. Xiang, E.G. Wang, and K. Han: *Mater. Res. Express*, 2022, vol. 9, p. 026530. https://doi.org/10.1088/2053-1591/ac5775.

28. D. Raabe, S. Ohsaki, and K. Hono: *Acta Mater.*, 2009, vol. 57, pp. 5254–63. https://doi.org/10.1016/j.actamat.2009.07.028.

29. S.G. Jia, P. Liu, F.Z. Ren, B.H. Tian, M.S. Zheng, and G.S. Zhou: *Met. Mater. Int.*, 2007, vol. 13, pp. 25–30. https://doi.org/10.1007/bf03027819.

30. G. Bao, Y. Xu, L. Huang, X. Lu, L. Zhang, Y. Fang, L. Meng, and J. Liu: *Mater. Res. Lett.*, 2016, vol. 4, pp. 37–42. https://doi.org/10.1080/21663831.2015.1091795.

31. D. Raabe and D. Mattissen: *Acta Mater.*, 1998, vol. 46, pp. 5973–84. https://doi.org/10.1016/S1359-6454(98)00218-3.

32. X. Huang, H. Sun, J. Shen, K. Cui, and G. Wang: *Materials*, 2019, vol. 12, p. 2990. https://doi.org/10.3390/ma12182990.

33. Y. Zhou, H. Zhao, and K. Zhang: *J. Less-Common Met.*, 1988, vol. 138, pp. 7–10. https://doi.org/10.1016/0022-5088(88)90230-5.

34. F. Bittner, S. Yin, A. Kauffmann, J. Freudenberger, H. Klauß, G. Korpala, R. Kawalla, W. Schillinger, and L. Schultz: *Mater. Sci. Eng. A*, 2014, vol. 597, pp. 139–47. https://doi.org/10.1016/j.msea.2013.12.051.

35. X. Wu, R. Wang, C. Peng, Y. Feng, and Z. Cai: *Mater. Des.*, 2019, vol. 168, p. 107676. https://doi.org/10.1016/j.matdes.2019.107676.

36. D.H. Kirkwood: *Mater. Sci. Eng.*, 1985, vol. 73, pp. L1–L4. https://doi.org/10.1016/0025-5416(85)90319-2.

37. J.B. Liu, L. Meng, and L. Zhang: *J. Alloys Compd.*, 2006, vol. 425, pp. 185–90. https://doi.org/10.1016/j.jallcom.2006.01.061.

38. P.H. Hu, H.W. Song, Y. Chen, F.P. Chen, and S.H. Zhang: *J. Alloys Compd.*, 2021, vol. 883, p. 160912. https://doi.org/10.1016/j.jallcom.2021.160912.

39. E.H. Kissinger: *Anal. Chem.*, 1957, vol. 29, pp. 1702–06. https://doi.org/10.1021/ac60131a045.

40. A.T. Adorno, R.A.G. Silva, and T.B. Neves: *Mater. Sci. Eng. A*, 2006, vol. 441, pp. 259–65. https://doi.org/10.1016/j.msea.2006.08.055.

41. D. Hamana: *Mater. Sci. Appl.*, 2011, vol. 02, pp. 899–910. https://doi.org/10.4236/msa.2011.27120.

42. X. Zuo, K. Han, C. Zhao, R. Niu, and E. Wang: *J. Alloys Compd.*, 2015, vol. 622, pp. 69–72. https://doi.org/10.1016/j.jallcom.2014.10.037.

43. X. Zuo, K. Han, C. Zhao, R. Niu, and E. Wang: *Mater. Sci. Eng. A*, 2014, vol. 619, pp. 319–27. https://doi.org/10.1016/j.msea.2014.09.070.

44. J.D. Verhoeven, H.L. Downing, L.S. Chumbley, and E.D. Gibson: *J. Appl. Phys.*, 1989, vol. 65, pp. 1293–1301. https://doi.org/10.1063/1.343024.

45. U. Hangen and D. Raabe: *Acta Metall. Mater.*, 1995, vol. 43, pp. 4075–82. https://doi.org/10.1016/0956-7151(95)00079-B.

46. S.I. Hong and M.A. Hill: *Mater. Sci. Eng. A*, 1999, vol. 264, pp. 151–58. https://doi.org/10.1016/s0921-5093(98)01097-1.

47. S.I. Hahn and S.J. Hwang: *J. Alloys Compd.*, 2009, vol. 483, pp. 207–08. https://doi.org/10.1016/j.jallcom.2008.07.205.

48. K. Han, J.D. Embury, J.R. Sims, L.J. Campbell, H.J. Schneider-Muntau, V.I. Pantsyrnyi, A. Shikov, A. Nikulin, and A. Vorobieva: *Mater. Sci. Eng. A*, 1999, vol. 267, pp. 99–114. https://doi.org/10.1016/S0921-5093(99)00025-8.

49. M.S. Lim, J.S. Song, and S.I. Hong: *J. Mater. Sci.*, 2000, vol. 35, pp. 4557–61. https://doi.org/10.1023/A:1004876806313.

50. T. Nizolek, I.J. Beyerlein, N.A. Mara, J.T. Avallone, and T.M. Pollock: *Appl. Phys. Lett.*, 2016, vol. 108, p. 051903. https://doi.org/10.1063/1.4941043.

51. L. Zhang, K. Han, T.N. Man, E.G. Wang, and X.W. Zuo: *J. Iron. Steel Res. Int.*, 2016, vol. 23, pp. 638–46. https://doi.org/10.1016/S1006-706X(16)30100-5.

52. K. Han, A.A. Vasquez, Y. Xin, and P.N. Kalu: *Acta Mater.*, 2003, vol. 51, pp. 767–80. https://doi.org/10.1016/s1359-6454(02)00468-8.

53. M. Xie, W. Huang, H. Chen, L. Gong, W. Xie, H. Wang, and B. Yang: *J. Alloys Compd.*, 2021, vol. 851, p. 156893. https://doi.org/10.1016/j.jallcom.2020.156893.

54. C. Zhao, X. Zuo, E. Wang, and K. Han: *Met. Mater. Int.*, 2017, vol. 23, pp. 369–77. https://doi.org/10.1007/s12540-017-6417-2.